

# Electronic band structure of $\text{CaSnN}_2$ : a sustainable alternative for blue LEDs.

Ilteris K. Turan,\* Sarker Md. Sadman,<sup>†</sup> and Walter R L. Lambrecht<sup>‡</sup>

*Department of Physics, Case Western Reserve University,  
10900 Euclid Avenue, Cleveland, OH 44106-7079, USA*

The electronic band structure of  $\text{CaSnN}_2$  in the wurtzite based  $Pna_2_1$  structure is calculated using the Quasiparticle Self-consistent (QS)  $GW^{\text{BSE}}$  method including ladder diagrams in the screened Coulomb interaction  $W^{\text{BSE}}$  and is found to have a direct gap of 2.680 eV at  $\Gamma$ , which corresponds to blue light wavelength of 463 nm and makes it an attractive candidate for sustainable blue light-emitting diodes (LEDs), avoiding Ga and In. The valence band maximum has  $a_1$  symmetry and gives allowed transitions to the conduction band minimum for light polarized along the  $\mathbf{c}$ -direction. The valence band splitting is analyzed in terms of symmetry labeling and the effective mass tensor is calculated for several bands at  $\Gamma$ . The optical dielectric function including electron-hole interaction effects is also reported and the excitons are analyzed, including several dark excitons.

## I. INTRODUCTION

The importance of the group-III nitrides, including AlN, GaN, InN and their alloys and hetero-structures, which form the basis of white light-emitting diodes and blue lasers, was recognized with the Nobel Prize in Physics of 2014 [1]. While work continues to increase the efficiency of these devices and to extend their operation into the deeper UV region, the problem of their sustainability is also gathering attention as both In and Ga become scarce and more expensive as their widespread use in semiconductors increases. The family of ternary II-IV-N<sub>2</sub> nitrides provide a potential solution to this problem with naturally abundant elements such as II=Mg, Zn, Ca and group IV=Si, Ge, Sn. While Ge is also less abundant, both Si and Sn are abundant elements [2]. The II-IV-N<sub>2</sub> semiconductors have been reviewed in [3–5] with the emphasis on Zn-based compounds. Recently, the Mg compounds have been investigated for their potential to achieve higher band gaps [6–11]. Among the Ca based compounds,  $\text{CaSiN}_2$  has been synthesized as early as 1924 [12–14] and  $\text{CaGeN}_2$  synthesis was reported since 1967 [15, 16], but besides the structure reports, its properties have not been much investigated. We are only aware of one band structure calculation of  $\text{CaSiN}_2$  [17]. More recently other alkaline earth silicon nitrides have been synthesized [18].

$\text{CaSnN}_2$  high pressure growth was reported by Kawamura *et al.* [19]. They found a rock-salt type structure with space group  $R\bar{3}m$ . On the other hand, the Materials Project lists  $\text{CaSnN}_2$  as having a wurtzite based  $Pna_2_1$  structure in entry mp-1029633 [20], but no information is provided on the electronic structure. Here we report computational predictions of  $\text{CaSnN}_2$  in the  $Pna_2_1$  structure, and predict a direct band gap in the blue range of the visible spectrum.  $\text{CaSnN}_2$  could thus be an attrac-

tive replacement for  $\text{In}_x\text{Ga}_{1-x}\text{N}$  in blue LEDs. Of course this will depend on the capability to grow the material in single crystal thin film form and on the capability of both p and n-type doping. In this paper, we focus only on the band structure and crystal structure of  $Pna_2_1$   $\text{CaSnN}_2$ .

## II. COMPUTATIONAL METHODS

Our calculations use the full-potential linearized muffin-tin orbital method (FP-LMTO) as implemented in the QUESTAAL codes, [21] which incorporates both Density Functional Theory (DFT) and Many-Body Perturbation Theory (MBPT). The DFT calculations of the structural stability are carried out in the PBEsol parametrization of the generalized gradient approximation to exchange and correlation [22]. To make accurate predictions of the band structure and in particular, the band gap we use the Quasiparticle Self-consistent  $GW$  (QSGW) [23, 24] method, which is a variant of Hedin's  $GW$  theory [25] in which  $G$  stands for the one-electron Green's function and  $W$  for the screened Coulomb interaction. In this quasiparticle self-consistent version, a non-local exchange correlation potential is extracted from the energy dependent  $GW$  self-energy  $\Sigma(\omega) = i\mathcal{G}W$  in each iteration and its off-diagonal elements in the basis set of the  $H^0$  Hamiltonian from which this  $G$  and  $W$  were derived is included in the next iteration until the self-energy no longer changes. This provides a  $GW$  result independent of the DFT starting point  $H^0$  and Kohn-Sham eigenvalues from the effective potential  $H^0$  which equal the real part of the quasiparticle excitation energies. The specific prescription for extracting the exchange correlation correction is

$$\Delta v_{xc} = \frac{1}{2} |\psi_i\rangle \text{Re} [\Sigma_{ij}(\epsilon_i) + \Sigma_{ij}(\epsilon_j)] \langle \psi_j|, \quad (1)$$

where summation over repeated indices is assumed. A more recent version of QSGW goes beyond the random phase approximation (RPA) in calculating the screened Coulomb interaction  $W(\mathbf{q}, \omega)$  by including electron-hole

\* ilteris.turan@case.edu

<sup>†</sup> sarker.sadman@case.edu

<sup>‡</sup> walter.lambrecht@case.edu

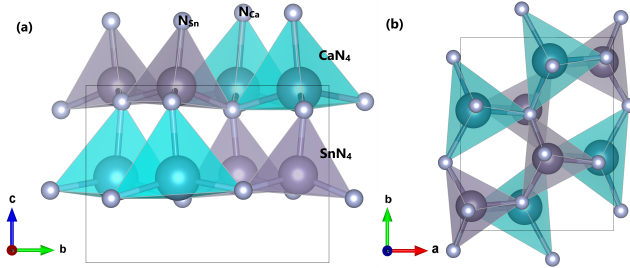


Fig. 1: Crystal structure of  $\text{CaSnN}_2$  with nearest neighbor  $\text{CaN}_4$  tetrahedra in blue and nearest neighbor  $\text{SnN}_4$  tetrahedra in gray shown from (a) side view and (b) top view. The image is generated using the VESTA3 software [31].

interactions or ladder diagrams in the polarization propagator via a Bethe-Salpeter Equation (BSE) approach [26]. It has been called  $\text{QSGW}$  or  $\text{QSGW}^{\text{BSE}}$  to distinguish it from  $\text{QSGW}^{\text{RPA}}$ .

The BSE are also used to investigate the optical properties in the long wavelength  $\mathbf{q} \rightarrow 0$  limit [27–29]. Here, we use the implementation in the LMTO and product basis set developed by Cunningham *et al.* [26, 30].

We use a *spdfspd* envelope basis set on Ca, S and N with augmentation up to  $l = 4$ . The Ca-3p and Sn-4d semi-core levels are treated as local orbitals. The self-energy matrix is approximated by a diagonal average value above a cut-off of 2.15 Ry. A  $5 \times 5 \times 5$   $\mathbf{k}$ -mesh is used to sample the Brillouin zone both for charge self-consistent calculations and to sample the self-energy.

The optical dielectric function is calculated using both the *independent (quasi)particle approximation* (IPA) and the Bethe Salpeter equation in the Tamm-Damcoff approximation and with static  $W$  [27] as implemented by Cunningham *et al.* [26] in LMTO basis set within the QUESTAAL suite. In the IPA, we find the imaginary part of the dielectric function,  $\varepsilon_2$ , by calculating the velocity matrix elements for direct transitions from the valence states  $\psi_{v\mathbf{k}}$  to conduction states  $\psi_{c\mathbf{k}}$  with energies  $\epsilon_{v\mathbf{k}}$ ,  $\epsilon_{c\mathbf{k}}$  in  $GW$ :

$$\varepsilon_2(\omega) = \frac{8\pi^2}{\Omega\omega^2} \sum_{cv\mathbf{k}} (f_{v\mathbf{k}} - f_{c\mathbf{k}}) |\langle \psi_{v\mathbf{k}} | \hat{e} \cdot \mathbf{v} | \psi_{c\mathbf{k}} \rangle|^2 \times \delta(\epsilon_{c\mathbf{k}} - \epsilon_{v\mathbf{k}} - \omega), \quad (2)$$

where  $\Omega$  is the unit cell volume,  $\hat{e}$  the polarization,  $\mathbf{v}$  the velocity operator, and  $f_{n\mathbf{k}}$  are Fermi occupation factors for the conduction bands  $c$  and valence bands  $v$ . The advantage of this approach is that we can carry out the Brillouin zone integrations using the tetrahedron method and use a well-converged  $\mathbf{k}$ -mesh. Also, it is possible to take the sum over bands apart into contributions from band pairs.

In the BSE in the Tamm-Dancoff approximation [27–29, 32], the dielectric function is similarly calculated from

the eigenvalues and eigenvectors of a two-particle Hamiltonian,

$$H_{n_1 n_2 \mathbf{k}, n'_1 n'_2 \mathbf{k}'}^{(2p)}(\mathbf{q}) = (\epsilon_{n_2 \mathbf{k}+\mathbf{q}} - \epsilon_{n_1 \mathbf{k}}) \delta_{n_1 n'_1} \delta_{n_2 n'_2} \delta_{\mathbf{k} \mathbf{k}'} - (f_{n_2 \mathbf{k}+\mathbf{q}} - f_{n_1 \mathbf{k}}) K_{n_1 n_2 \mathbf{k}, n'_1 n'_2 \mathbf{k}'}(\mathbf{q}), \quad (3)$$

with  $f_{n\mathbf{k}}$  the Fermi occupation function for band  $n$  at  $\mathbf{k}$ , which includes the electron-hole interactions kernel  $K_{n_1 n_2 \mathbf{k}, n'_1 n'_2 \mathbf{k}'}(\mathbf{q})$  expanded in the basis of one-particle eigenstates  $\psi_{n\mathbf{k}}(\mathbf{r})$ . This effectively mixes the direct vertical band to band transitions  $(\epsilon_{c\mathbf{k}} - \epsilon_{v\mathbf{k}})$  at different  $\mathbf{k}$  into new “exciton” eigenstates  $E^\lambda$  [33]. Diagonalizing this Hamiltonian in the Tamm-Dancoff approximation, where  $n_1$  is restricted to be a valence state and  $n_2$  a conduction band state, one obtains the exciton eigenvalues  $E^\lambda(\mathbf{q})$  and eigenvectors  $A_{n_1 n_2 \mathbf{k}}^\lambda(\mathbf{q})$ , *i.e.*  $A_{v\mathbf{c}\mathbf{k}}^\lambda(\mathbf{q})$ . Furthermore, excitonic band weight contributions,  $W_{c\mathbf{k}} = \sum_v |A_{v\mathbf{c}\mathbf{k}}^\lambda(\mathbf{q})|^2$  and  $W_{v\mathbf{k}} = \sum_c |A_{v\mathbf{c}\mathbf{k}}^\lambda(\mathbf{q})|^2$ , for a given conduction  $c\mathbf{k}$  and valence  $v\mathbf{k}$  band of the two-particle states in a narrow energy range  $E_{\min} \leq E^\lambda(\mathbf{q}) \leq E_{\max}$ , can be obtained from the exciton eigenvectors. Here  $\lambda$  denotes the excitonic eigenstate.

In addition, the macroscopic dielectric function is then given by

$$\varepsilon_M(\omega) = 1 - \lim_{\mathbf{q} \rightarrow 0} \frac{8\pi}{|\mathbf{q}|^2 \Omega N_k} \sum_{ss'} (f_{n'_2 \mathbf{k}'+\mathbf{q}} - f_{n'_1 \mathbf{k}'}) \rho_s(\mathbf{q}) \sum_\lambda \frac{A_s^\lambda(\mathbf{q}) A_{s'}^{\lambda*}(\mathbf{q})}{E^\lambda(\mathbf{q}) - \omega \pm i\eta} \rho_{s'}(\mathbf{q})^*, \quad (4)$$

introducing the shorthand  $s = \{n_1 n_2 \mathbf{k}\}$ , with the matrix elements,

$$\rho_{n_1 n_2 \mathbf{k}}(\mathbf{q}) = \langle \psi_{n_2 \mathbf{k}+\mathbf{q}} | e^{i\mathbf{q} \cdot \mathbf{r}} | \psi_{n_1 \mathbf{k}} \rangle. \quad (5)$$

Here, we assumed a non-spin polarized case, with a factor two included for spin and  $N_k$  is the number of  $\mathbf{k}$ -points in the Brillouin zone.

We note that neither of these methods include indirect band to band transitions assisted by electron-phonon coupling or the corrections due to zero-point-motion. These are estimated to be of order -0.1 to -0.2 eV [34, 35]. In the present case, we notice that the lowest gap is direct so the neglect of indirect transitions is of no concern.

Finally, the effective mass tensor elements,  $M_{\alpha\beta}^{-1}$  can be calculated from the one-particle states  $|\psi_{n\mathbf{k}}\rangle$ ,  $\epsilon_{n\mathbf{k}}$ , within the  $\mathbf{k} \cdot \mathbf{p}$  theory:

$$(\mathbf{M}^{-1})_{\alpha\beta} = \delta_{\alpha\beta} \frac{1}{m_e} + \frac{1}{m_e^2} \times \sum_{n_2 \neq n_1} \frac{\langle \psi_{n_1 \mathbf{k}} | \hat{\mathbf{p}}_\alpha | \psi_{n_2 \mathbf{k}} \rangle \langle \psi_{n_2 \mathbf{k}} | \hat{\mathbf{p}}_\beta | \psi_{n_1 \mathbf{k}} \rangle + \text{c.c.}}{\epsilon_{n_1 \mathbf{k}} - \epsilon_{n_2 \mathbf{k}}}, \quad (6)$$

where  $m_e$  is the electron mass,  $\hat{\mathbf{p}}_{\alpha,\beta}$  are components of the momentum operator, and c.c. stands for the complex conjugate of the preceding terms.

### III. RESULTS

The crystal structure is shown in Fig.1. It belongs to the space-group number 33,  $Pna2_1$  or  $C_{2v}^9$ . We use the symmetrized primitive cell containing 16 atoms obtained from the Materials Project (MP) [36], item mp-1029633 [20]. The structural lattice parameters are  $a = 6.124 \text{ \AA}$ ,  $b = 7.719 \text{ \AA}$ , and  $c = 5.619 \text{ \AA}$ . Each type of atom sits at the  $4a$  Wyckoff position in the primitive unit cell with  $(x, y, z)_{\text{Ca}} = (0.083, 0.623, 0.977)$ ,  $(x, y, z)_{\text{Sn}} = (0.069, 0.127, 0.994)$ ,  $(x, y, z)_{\text{N}_{\text{Ca}}} = (0.048, 0.103, 0.362)$ , and  $(x, y, z)_{\text{N}_{\text{Sn}}} = (0.100, 0.647, 0.408)$  in reduced coordinates.

We note that the ratio  $a/b = 0.793$  is significantly smaller than the ideal  $\sqrt{3}/2 = 0.866$  of the wurtzite supercell. We can define the equivalent wurtzite lattice constant by the area of the unit cell in the basal plane  $a_w^2 2\sqrt{3} = ab$ , which gives  $a_w = 3.693 \text{ \AA}$ . The wurtzite type  $c/a_w$  is then 1.521 which is much smaller than the ideal ratio of  $\sqrt{8/3} \approx 1.633$ . In fact it is even lower than that of AlN, where the  $c/a$  is 1.602. There is thus a strong distortion due to the large difference in ionic radii of Sn (Shannon radius 0.55 for four-fold coordination) and Ca (Shannon radius 1 for six-fold coordination). As we will show later, this has an important impact for the crystal field splitting of the valence band maximum.

#### A. Band Structures

TABLE I: Band gaps within various computational levels at the  $\Gamma$  point in  $Pna2_1$   $\text{CaSnN}_2$ .

transition	gap (eV)		
	GGA	$G^0W^0$	$\text{QSGW}^{\text{RPA}}$
$\Gamma - \Gamma$	1.352	2.438	2.776
			2.680

The band structure in the  $\text{QSGW}^{\text{BSE}}$  approach is shown in Fig. 2. The band gap in the  $\text{QSGW}^{\text{BSE}}$  is 2.680 eV which corresponds to  $\lambda = hc/E_g$  of 463 nm in the blue region of the visible spectrum. The band gaps in different computational approximations are given in Table I. We can see that the gap in  $\text{QSGW}^{\text{RPA}}$  is somewhat larger than in  $\text{QSGW}^{\text{BSE}}$ , while the  $G^0W^0$  gap, which gives the first iteration result after the GGA, is smaller but still significantly larger than the GGA. Note that the  $G^0W^0$  already includes off-diagonal elements of the  $\Sigma$  self-energy and thus differs from the usual single-shot perturbative  $G^0W^0$ . The gap correction from GGA to  $\text{QSGW}^{\text{RPA}}$  is reduced by a factor 0.92 when going to  $\text{QSGW}^{\text{BSE}}$ . This correction is somewhat sensitive to the number of bands included in the BSE treatment of the  $W^{\text{BSE}}(\mathbf{q}, \omega)$ . If instead of  $\text{QSGW}^{\text{BSE}}$  we rescale the self-energy of  $\text{QSGW}^{\text{RPA}}$  by the usual 0.8 reduction factor, we obtain a gap of 2.49 eV, which still corresponds to the blue-green region. There remains some uncertainty

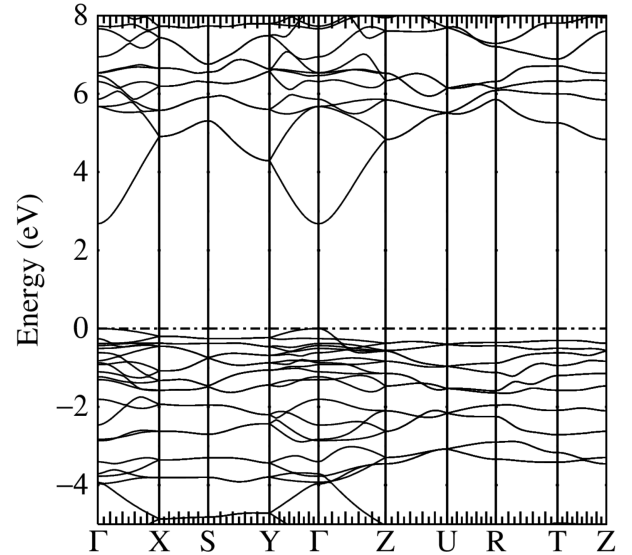


Fig. 2: Band structure of  $\text{CaSnN}_2$  obtained in the  $\text{QSGW}^{\text{BSE}}$  method, the irreducible Brillouin zone is a rectangular box with corners  $\Gamma = (0, 0, 0)$ ,  $X = (\pi/a, 0, 0)$ ,  $Y = (0, \pi/b, 0)$ ,  $S = (\pi/a, \pi/b, 0)$ ,  $Z = (0, 0, \pi/c)$ ,  $U = (\pi/a, 0, \pi/c)$ ,  $T = (0, \pi/b, \pi/c)$ ,  $R = (\pi/a, \pi/b, \pi/c)$ .

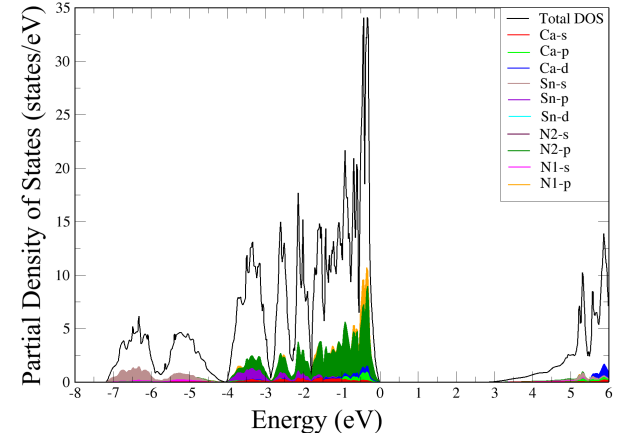


Fig. 3: Total and partial densities of states in  $Pna2_1$   $\text{CaSnN}_2$ . The partial contributions include the sum over all equivalent atoms, but refer to partial wave contributions inside the muffin-tin spheres only, excluding those from the interstitial region and only showing the major contributions. Here  $N_1$  are the Nitrogen labeled as  $\text{N}_{\text{Ca}}$ , and  $N_2$  are  $\text{N}_{\text{Sn}}$  in Fig. 1.

of order 0.1 eV on this gap because of the zero-point motion correction which would lower the gap and because the PBE lattice constant may be slightly overestimated which could lead to an underestimate of the gap.

In Fig. 2, we can see that the minimum gap is direct at  $\Gamma$ . The conduction band minimum (CBM) shows a strong dispersion, characteristic of a small effective mass. The

TABLE II: Symmetry labeled energy levels at  $\Gamma$  relative to VBM within QSGW<sup>BSE</sup> for the bottom three conduction bands and top six valence bands.

Level	Symmetry	Energy (eV)
CBM+2	$b_2$	5.680
CBM+1	$b_1$	5.678
CBM	$a_1$	2.680
VBM	$a_1$	0
VBM-1	$b_1$	-0.257
VBM-2	$a_2$	-0.380
VBM-3	$b_1$	-0.434
VBM-4	$b_2$	-0.505
VBM-5	$a_1$	-0.615

valence band maximum (VBM) occurs at  $\Gamma$  and has its strongest dispersion along  $\Gamma Z$ . As explained in [37], this indicates that the VBM has  $a_1$  as irreducible symmetry representation, because  $z$  corresponds to  $a_1$ . Since the conduction band minimum is  $s$  like in character and also of  $a_1$  symmetry, the transitions from the top VBM to the CBM are allowed for  $\mathbf{E} \parallel \mathbf{c}$  or  $z$ -polarization. This is similar to AlN and is somewhat disadvantageous for normal incidence light extraction for basal plane oriented films but not if the films would have the  $c$ -plane in the plane of the film. This orientation is actually found to occur for growth of other II-IV-N<sub>2</sub>, for example ZnSiN<sub>2</sub> [38], on  $r$ -plane sapphire. The next valence band separated by a crystal field splitting of 0.257 eV has its smallest mass along  $\Gamma X$  and is thus of  $x$  or  $b_1$  symmetry and has allowed transitions to the CBM for  $\mathbf{E} \parallel \mathbf{a}$ . We confirmed these irreducible symmetry labeling by inspection of the eigenvectors. We give the symmetry labels and values relative to the VBM of a few valence and conduction bands near the gap in Table II. We can see that only the VBM-4 has the  $b_2$  or  $y$ -like character and two other states, one with  $a_2$  and another one with  $b_1$  symmetry lie in between. In the conduction band, the next two higher levels at  $\Gamma$  are very close to each other.

The effective mass tensor components are given in Table III. Because of the orthorhombic symmetry, the effective mass tensor is diagonal but with different values in each of the Cartesian directions. We can see that the CBM has almost isotropic symmetry, while the valence bands have quite different masses in different directions. Note that the VBM-1 has one of its mass tensor components of positive sign and two of negative sign, meaning that it is a saddle point instead of a maximum. The VBM-2 corresponding to  $a_2$  symmetry has very flat band and hence high effective hole mass. The VBM-4 has its smallest negative mass along the  $y$  direction, consistent with its  $b_2$  symmetry. The CBM+1 and CBM+2 again are saddle point like as one can also directly see in the band structure Fig.2. The effective mass tensor can qualitatively be understood from Eq. 6. The closer the energy  $\epsilon_{n_2\mathbf{k}}$  of band  $n_2\mathbf{k}$  is to the energy  $\epsilon_{n_1\mathbf{k}}$  of band  $n_1\mathbf{k}$ , the larger the deviation of the inverse effective mass

TABLE III: Effective mass tensor components in atomic units for the bottom three conduction bands and top six valence bands at the  $\Gamma$  point.

Level	$M_{xx}$	$M_{yy}$	$M_{zz}$
CBM+2	-0.248	-0.434	1.525
CBM+1	-0.785	6.468	-0.278
CBM	0.224	0.208	0.252
VBM	-5.824	-3.010	-0.270
VBM-1	-0.331	2.605	-9.810
VBM-2	-48.710	13.843	-0.819
VBM-3	-4.233	1.934	-0.980
VBM-4	-4.519	-0.884	8.488
VBM-5	-2.228	-0.675	2.053

from  $1/m_e$  will be. A nearby band of higher energy tends to make the effective mass negative, while a nearby band of lower energy tends to make the effective mass positive. On the other hand, as an example, the top valence band of  $a_1$  symmetry only can couple to the higher lying  $a_1$  symmetry for the  $p_z$  operator in the matrix elements and this explains why the largest negative dispersion occurs along  $\Gamma Z$ , likewise for the next VBM-1 of  $b_1$  character. The momentum matrix elements are larger between the valence bands and the lowest conduction band than to lower lying valence bands because of the atomic orbital character of the bands involved. The coupling to the higher conduction bands plays less of a role because for these the energy denominators in Eq.6 become large.

The Partial Densities of States (PDOS) are given in Fig.3. We can see that down to about 4 eV below the VBM the states have mostly N- $p$  character with both  $N_1 = N_{Ca}$  and  $N_2 = N_{Sn}$  giving almost equal contributions. As we move deeper into the VBM, the N- $s$  play a larger role and hybridization with Sn and Ca increases as the states become stronger bonding in character. The analysis of the bands' atomic orbital contributions shows that the CBM is mostly Sn- $s$ -like. The Ca- $d$  states show up in the CBM at about 6 eV and as bonding states at about 0.5 eV below the VBM.

## B. Optical Properties

The imaginary part of the dielectric function  $\epsilon_2(\omega)$  is shown in Fig. 4. Because of the orthorhombic symmetry, the tensor has three independent components. We show the results both in the independent particle approximation (IPA) and the Bethe Salpeter Equation (BSE) approach. The former does not include local field nor electron-hole interaction effects while the latter does include both. We here use a fairly small and energy independent broadening factor (imaginary part  $\eta$  in the denominator) to show the excitonic peaks clearly below the quasiparticle gap, indicated by the vertical line. In reality we may expect that the lifetime broadening would increase with energy.

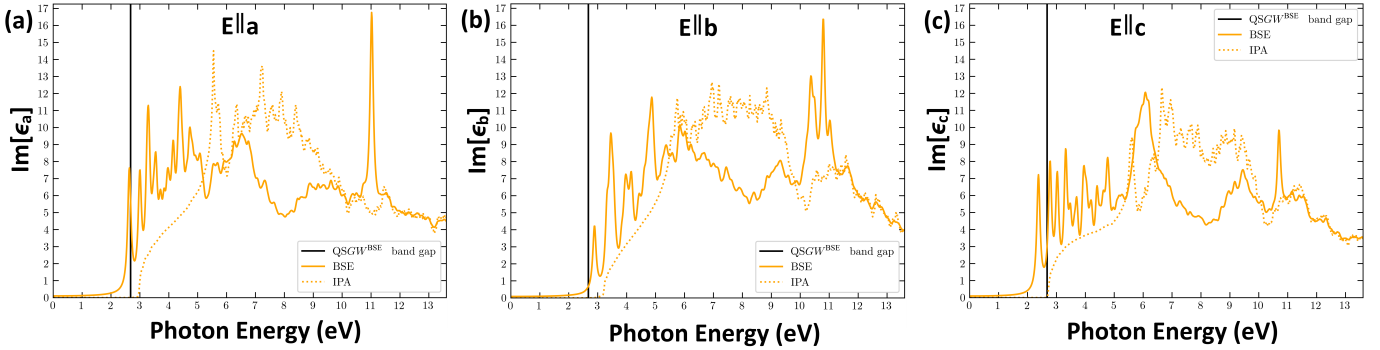


Fig. 4: Imaginary part of the optical dielectric function,  $\varepsilon_2^i(\omega)$  shown in full line, obtained using the BSE with the broadening parameter of  $\eta = 0.005$  Ry (as in Eq. 4), including top 15 valence bands and bottom 13 conduction bands. Independent particle approximation results using a finer  $20 \times 20 \times 20$   $\mathbf{k}$ -point mesh, without any broadening factor (as in Eq. 2) is shown in dotted line. The three components of the macroscopic dielectric function parallel to **a**, **b**, **c** axes are shown in (a), (b), (c) respectively.

We can see that the lowest excitonic peak occurs for the  $\mathbf{E} \parallel \mathbf{c}$  polarization, in agreement with our comments about the symmetry labeling of the corresponding bands and allowed transitions in the previous section. The exciton for  $\mathbf{E} \parallel \mathbf{a}$  has the next higher energy and lies still below the quasiparticle gap while the exciton for  $\mathbf{E} \parallel \mathbf{b}$  lies already above the quasiparticle gap. However, since this exciton is derived from a valence band below the VBM, it still has a binding energy relative to the direct gap for that polarization.

The lowest few exciton eigenvalues are given in Table IV along with their oscillator strength relative to the first bright one, their polarization and the band of corresponding symmetry from which they are derived. In Fig. 5 the band weights  $W_{v\mathbf{k}}$  and  $W_{c\mathbf{k}}$  are given as colored dots with the size of the dots indicating the weight on the band structure for some of the low lying excitons. We can indeed see that all the excitons shown here are derived from the conduction band minimum at  $\Gamma$  but different excitons derive from different valence bands. The lowest exciton, which is polarized along  $z$  is derived mostly from the top valence band, while the next one is derived from the VBM-1. The third exciton at 2.754 eV is derived from VBM-2 which has  $a_2$  band symmetry and therefore gives a dark exciton. The fourth exciton at 2.782 eV is again derived from the top valence band, consistent with its  $z$  polarization, but shows higher contribution away from  $\Gamma Y$  then at  $\Gamma$ . This indicates it could have a radial node in  $\mathbf{k}$ -space and real space as in a  $2s$ -like hydrogenic function. This excited exciton state already lies above the corresponding band gap. The exciton at 2.803 eV is also derived from the top VBM but has an oscillator weight two orders of magnitude less than  $\lambda = 4$  exciton. Namely, this exciton has weight primarily along  $\Gamma Y$  only and thus the  $xy$  plane is a nodal plane. This corresponds to a  $p_y$ -like hydrogenic envelope function. The  $A_{vc\mathbf{k}}^\lambda$  for a given band pair  $vc$  as function of  $\mathbf{k}$  is the Fourier transform of a slowly varying envelope function in the hydrogenic model and can thus have different

TABLE IV: Exciton eigenvalues ( $E^\lambda$ ), oscillator strengths ( $S^\lambda$ ) relative to that of the first bright one, polarizations ( $\hat{e}$ ) if bright, symmetries of the corresponding valence bands, the band energies ( $\epsilon_c - \epsilon_v$ ), and exciton binding energies ( $E_B$ ). All energies are given in eV.

$\lambda$	$E^\lambda$	$S^\lambda$	$\hat{e}$	sym	$\epsilon_c - \epsilon_v$	$E_B$
1	2.380	1	$z$	$a_1$	2.680	0.300
2	2.636	1.04	$x$	$b_1$	2.937	0.301
3	2.754	0	dark	$a_2$	3.060	0.306
4	2.782	1.05	$z$	$a_1$	2.680	-0.102
5	2.803	0.01	$y$	$b_2$	3.185	0.382
6	2.813	0	dark	$a_1$	2.680	-0.133
7	2.891	0.56	$y$	$b_2$	3.185	0.294
8	2.984	0	dark	$a_1$	3.295	0.311
9	3.000	0.93	$x$	$b_1$	3.114	0.114

spherical harmonic character. In the present case, the hydrogenic model needs to be modified to incorporate the anisotropies resulting from the valence band symmetry and the screened Coulomb interaction. The fifth exciton at 2.803 eV is  $y$ -polarized but with a rather small oscillator strength. Interestingly, it has a higher binding energy. The exciton  $\lambda = 7$  at 2.891 eV is derived from VBM-4 and  $y$ -polarized. We note that this exciton lies above the nominal quasiparticle gap, indicated by the vertical lines in Fig.4 but below the  $y$ -polarization onset of the IPA  $\varepsilon_2$  which is at  $2.680 + 0.505 = 3.185$  eV. The exciton  $\lambda = 8$  at 2.984 eV is dark and is derived from VBM-5 of  $a_1$  symmetry.

One can see that the exciton binding energies measured from their corresponding band gap based on their symmetry assignment are pretty close to each other at about 0.3 eV but the dark exciton for  $\lambda = 6$ , which is an excited exciton state corresponding to the VBM-CBM band pair with a  $p$ -like envelope function, has in fact a negative binding energy relative to the corresponding

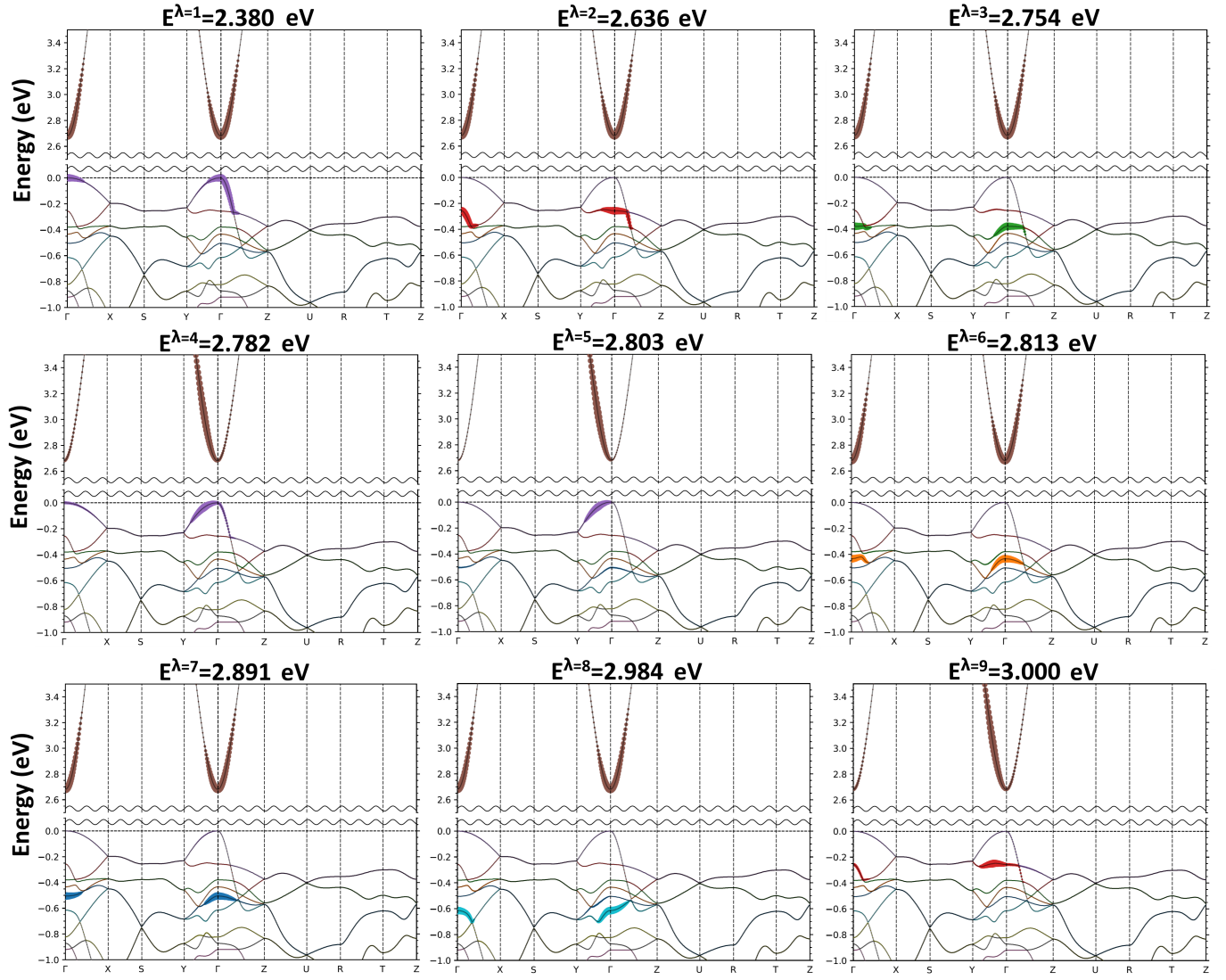


Fig. 5: Exciton wave function weights,  $W_{v(c)\mathbf{k}}^\lambda$ , for  $\lambda = 1 \dots 7$  contributed by CBM of  $a_1$  symmetry and top six valence bands of  $a_1$ ,  $b_1$ ,  $a_2$ ,  $b_1$ ,  $b_2$ , and  $a_1$  symmetries. The size of the colored circles are scaled with respect to the exciton weights, and the use of different colors serves to distinguish different bands. The  $\lambda = 3, 6, 8$  excitons are dark excitons, whereas the others are bright or semi-bright with respect to their oscillator strengths reported in Table IV.

gap. However, the binding energies obtained here are likely to be an overestimate for two reasons. First accurate binding energies require a dense  $\mathbf{k}$ -point mesh near the  $\Gamma$ -point from which the excitons are derived in a hydrogenic approximation. We can see indeed that the excitons have band weights from a narrow range near  $\Gamma$  and thus require a fine sampling near this point. Second, our calculation does not include phonon or lattice polarization effects in the dielectric screening. Typically, this will reduce the exciton binding energies by an order of magnitude [37]. This is because in the hydrogenic model the binding energy is inversely proportional to the dielectric constant squared: the Coulomb energy is screened by the dielectric constant and the effective Bohr radius is proportional to the dielectric constant. Thus, if we replace

the electronic screening only  $\varepsilon_\infty$  by the static dielectric constant  $\varepsilon_0$  including phonon contributions, the binding energies are divided by  $(\varepsilon_0/\varepsilon_\infty)^2$ .

The extrapolation result for the  $\lambda = 1$  exciton with  $a_1$  symmetry can be seen in Fig. 6, where we show the converged  $E^{\lambda=1}$  results as a function of inverse of the number of  $\mathbf{k}$  points in the Brillouin zone. Here we used  $N_k \times N_k \times N_k$  meshes with  $N_k \in \{4, 5, 6, 8, 10\}$ . We confirm that it is indeed important to converge the  $\mathbf{k}$ -point mesh used in the BSE two-particle Hamiltonian  $H_{v\mathbf{ck},v'\mathbf{c}'\mathbf{k}'}$  [39]. The extrapolated result of  $E^{\lambda=1} = 2.545$  eV, would correspond to a binding energy of  $E_B = 0.135$  eV. Additionally, we obtain the following static and macroscopic dielectric function results from density functional perturbation theory [40, 41] using the ABINIT code suite [42, 43]:

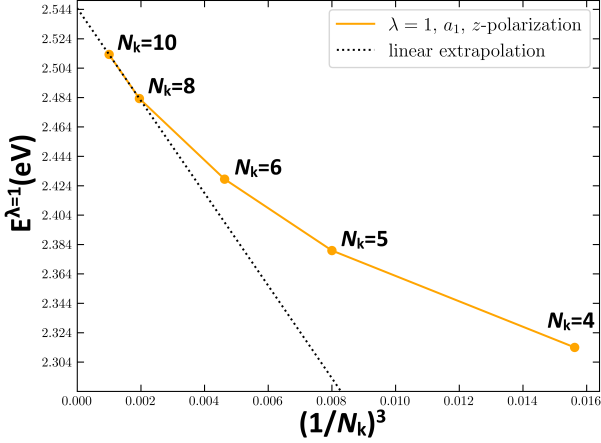


Fig. 6: Exciton energy levels for  $\lambda = 1$ , for  $a_1$  symmetry with  $z$ -polarization, as a function of  $\mathbf{k}$ -mesh density.

The extrapolated value is 2.545 eV.

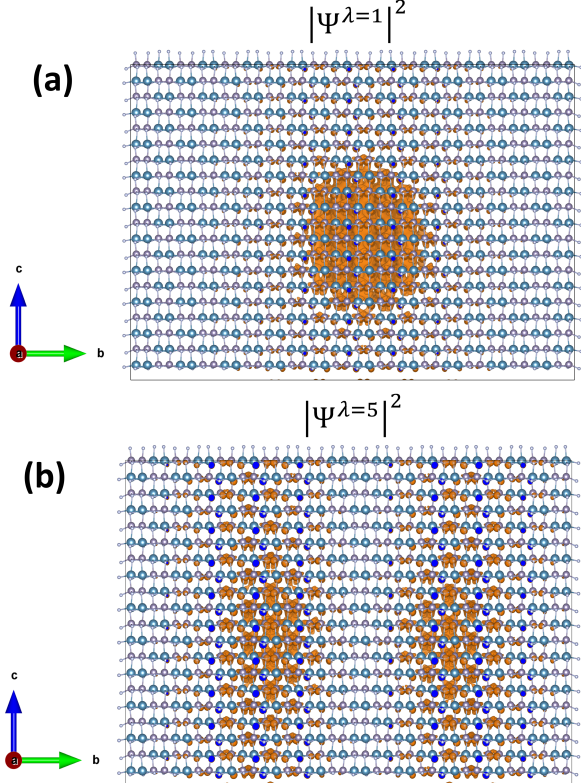


Fig. 7: Position space probability density  $|\Psi^\lambda((x, y, z)_{N_{Ca}}, \mathbf{r}_e)|^2$  of the (a)  $\lambda = 1$  and (b)  $\lambda = 5$  excitons, for a fixed hole position at  $(x, y, z)_{N_{Ca}}$ , confined within an extended cell of  $10 \times 10 \times 10$  the unit cell. Both cells are viewed from the side. The coloring of atomic sites is the same as in Fig. 1 and the probability density bubbles are shown in orange; the dark blue regions are the interior parts of the probability densities when they are cut by the supercell boundary.

$$\varepsilon_\infty = \begin{pmatrix} 6.3 & 0 & 0 \\ 0 & 5.8 & 0 \\ 0 & 0 & 6.2 \end{pmatrix}; \varepsilon_0 = \begin{pmatrix} 11.5 & 0 & 0 \\ 0 & 10.3 & 0 \\ 0 & 0 & 13.7 \end{pmatrix},$$

and from which we find the averaged values of  $\varepsilon_{\infty,0}^{\text{avg.}} = (\varepsilon_{\infty,0}^{\text{xx}} \times \varepsilon_{\infty,0}^{\text{yy}} \times \varepsilon_{\infty,0}^{\text{zz}})^{1/3}$ . Details of the phonon calculations used to obtain the static dielectric constant will be presented elsewhere.

Thus, when we further correct the extrapolated value by dividing with a factor of  $(\varepsilon_0^{\text{avg.}}/\varepsilon_\infty^{\text{avg.}})^2 \simeq 3.7$ , we obtain a binding energy of 36.6 meV, which is close to the known value in GaN. The higher lying excitons undergo similar corrections when using a finer  $\mathbf{k}$ -mesh but the relation to the band pairs and envelope function character remains the same,

We can further check the nature of some of the excitons by examining their wavefunction in real space. The exciton wave function is given by

$$\Psi^\lambda(\mathbf{r}_h, \mathbf{r}_e) = \sum_{vck} A_{vck}^\lambda \psi_{vck}(\mathbf{r}_h) \psi_{ck}(\mathbf{r}_e) \quad (7)$$

and we can look at  $|\Psi^\lambda(\mathbf{r}_h, \mathbf{r}_e)|^2$  as function of the electron position  $\mathbf{r}_e$  for a chosen position of the hole  $\mathbf{r}_h$ . Since the transitions are mostly between holes on N to the CBM, we pick the hole on a N site. The electron distribution for the first bright exciton is shown in Fig. 7(a) and is found to be quite spread out consistent with the shallow Wannier-type exciton. For the fifth exciton shown in Fig. 7(b) at 2.803 eV, we can indeed see a nodal plane consistent with the  $p_y$  like envelope function mentioned earlier.

#### IV. CONCLUSIONS

In this paper we showed that  $Pna2_1$  CaSnN<sub>2</sub> is potentially a useful semiconductor made of sustainable and abundant elements because it has a direct gap in the blue range of the visible spectrum. It is thus a potential alternative to  $In_xGa_{1-x}N$  which is currently used for blue LEDs and for the technology of adding a yellow phosphorescent coating for white LEDs. The predictions of the band gap were here done with an accurate and reliable method, the quasiparticle self-consistent QSGW<sup>BSE</sup> method, which includes electron-hole interaction effects in the screening of  $W$ . We find that the small  $c/a$  ratio of this compound leads to the VBM having  $z$  character and hence gives smallest exciton gap with polarization parallel to the  $\mathbf{c}$  axis. This is unfavorable for extraction of light from the basal plane but not if the film is grown with the  $\mathbf{c}$  axis in the plane of the film as would likely occur for growth on r-plane sapphire. There is a large crystal field splitting of 257 meV to the next lower valence band at  $\Gamma$  which is  $\mathbf{a}$  polarized. We presented also the effective mass tensor components for these bands, as well as a detailed analysis of the symmetry and binding energies of the excitons.

## ACKNOWLEDGMENTS

We wish to thank Professor K. Kash for bringing our attention to  $\text{CaSnN}_2$  and for many invaluable conversations. This work was supported by the US Air Force Office of Scientific Research (AFOSR) under grant No. FA9550-26-1-0005 and made use of the High Performance

Computing Resource in the Core Facility for Advanced Research Computing at Case Western Reserve University.

## DATA AVAILABILITY

The data that support the findings of this article are openly available [44]. Embargo periods may apply.

---

[1] (2014), the Nobel Prize in Physics 2014. NobelPrize.org. Nobel Prize Outreach 2025. Fri. 19 Dec 2025. <https://www.nobelprize.org/prizes/physics/2014/summary/>.

[2] <https://pubs.usgs.gov/fs/2002/fs087-02/>.

[3] W. R. L. Lambrecht and A. Punya, Heterovalent ternary II-IV-N<sub>2</sub> compounds: perspectives for a new class of wide-band-gap nitrides, in *III-Nitride Semiconductors and their Modern Devices*, edited by B. Gill (Oxford University Press, 2013) Chap. 15, pp. 519–585.

[4] S. Lyu, D. Skachkov, K. Kash, E. W. Blanton, and W. R. L. Lambrecht, Band Gaps, Band-Offsets, Disorder, Stability Region, and Point Defects in II-IV-N<sub>2</sub> Semiconductors, *physica status solidi (a)* **216**, 1800875 (2019).

[5] A. D. Martinez, A. N. Fioretti, E. S. Toberer, and A. C. Tamboli, Synthesis, structure, and optoelectronic properties of II-IV-V<sub>2</sub> materials, *J. Mater. Chem. A* **5**, 11418 (2017).

[6] A. P. Jaroenjittichai and W. R. L. Lambrecht, Electronic band structure of Mg–IV–N<sub>2</sub> compounds in the quasiparticle-self-consistent *GW* approximation, *Phys. Rev. B* **94**, 125201 (2016).

[7] S. Lyu and W. R. Lambrecht, Quasiparticle self-consistent *GW* band structures of Mg-IV-N<sub>2</sub> compounds: The role of semicore d states, *Solid State Communications* **299**, 113664 (2019).

[8] J. B. Quirk, M. Råsander, C. M. McGilvery, R. Palgrave, and M. A. Moram, Band gap and electronic structure of MgSiN<sub>2</sub>, *Applied Physics Letters* **105**, 112108 (2014).

[9] F. Arab, F. A. Sahraoui, K. Haddadi, A. Bouhemadou, and L. Louail, Phase stability, mechanical and thermodynamic properties of orthorhombic and trigonal MgSiN<sub>2</sub>: an ab initio study, *Phase Transitions: A Multinational Journal* **89**, 480 (2016).

[10] R. Bruls, H. Hintzen, R. Metselaar, and C.-K. Loong, Anisotropic thermal expansion of mgsin2 from 10 to 300 k as measured by neutron diffraction, *Journal of Physics and Chemistry of Solids* **61**, 1285 (2000).

[11] S. Pramchu, A. P. Jaroenjittichai, and Y. Laosiritaworn, Phonon and phonon-related properties of mgsin2 and mggen2 ceramics: First principles studies, *Ceramics International* **43**, S444 (2017), the 10th Asian Meeting on Electroceramics (AMEC-10).

[12] L. Wöhler and O. Bock, Das Silicium-Analogon des Kalkstickstoffs, *Zeitschrift für anorganische und allgemeine Chemie* **134**, 221 (1924).

[13] H. H. Franck and V. Louis, Calciumsilicide und Stickstoff, *Zeitschrift für anorganische und allgemeine Chemie* **242**, 128 (1939).

[14] Y. Laurent, Contribution à l'étude des systèmes calcium-azote et calcium-silicium-azote, *Rev. Chim. Min.* **5**, 1019 (1968).

[15] J. Guyader and J. Lang, Étude du système  $\text{Ca}_3\text{N}_2$ - $\text{Ge}_3\text{N}_4$ , *Rev. Chim. Min.* **3**, 937 (1967).

[16] M. Maunaye, J. Guyader, Y. Laurent, and J. Lang, Étude structurale de  $\text{CaGeN}_2$  et  $\text{Ca}_{1-x}\text{GeN}_2$ , *Bulletin de la Société Francaise de Minéralogie et de Cristallographie* **94**, 347 (1971).

[17] T. de Boer, T. D. Boyko, C. Braun, W. Schnick, and A. Moewes, Bandgap and electronic structure of CaSiN<sub>2</sub>: Experiment and theory, *International Journal of Applied Ceramic Technology* **20**, 197 (2023).

[18] Z. A. Gál, P. M. Mallinson, H. J. Orchard, and S. J. Clarke, Synthesis and Structure of Alkaline Earth Silicon Nitrides: BaSiN<sub>2</sub>, SrSiN<sub>2</sub>, and CaSiN<sub>2</sub>, *Inorganic Chemistry* **43**, 3998 (2004), pMID: 15206881.

[19] F. Kawamura, H. Murata, M. Imura, N. Yamada, and T. Taniguchi, Synthesis of CaSnN<sub>2</sub> via a High-Pressure Metathesis Reaction and the Properties of II-Sn-N<sub>2</sub> (II = Ca, Mg, Zn) Semiconductors, *Inorganic Chemistry* **60**, 1773 (2021), pMID: 33480682.

[20] <https://next-gen.materialsproject.org/materials/mp-1029633?formula=CaSnN2>.

[21] D. Pashov, S. Acharya, W. R. Lambrecht, J. Jackson, K. D. Belashchenko, A. Chantis, F. Jamet, and M. van Schilfgaarde, Questaal: A package of electronic structure methods based on the linear muffin-tin orbital technique, *Computer Physics Communications* , 107065 (2019).

[22] J. P. Perdew, A. Ruzsinszky, G. I. Csonka, O. A. Vydrov, G. E. Scuseria, L. A. Constantin, X. Zhou, and K. Burke, Restoring the Density-Gradient Expansion for Exchange in Solids and Surfaces, *Phys. Rev. Lett.* **100**, 136406 (2008).

[23] M. van Schilfgaarde, T. Kotani, and S. Faleev, Quasiparticle Self-Consistent *GW* Theory, *Phys. Rev. Lett.* **96**, 226402 (2006).

[24] T. Kotani, M. van Schilfgaarde, and S. V. Faleev, Quasiparticle self-consistent *GW* method: A basis for the independent-particle approximation, *Phys. Rev. B* **76**, 165106 (2007).

[25] L. Hedin, New method for calculating the one-particle green's function with application to the electron-gas problem, *Phys. Rev.* **139**, A796 (1965).

[26] B. Cunningham, M. Grüning, D. Pashov, and M. van Schilfgaarde, QSG *W*: Quasiparticle self-consistent *GW* with ladder diagrams in *W*, *Phys. Rev. B* **108**, 165104 (2023).

[27] G. Onida, L. Reining, and A. Rubio, Electronic excitations: density-functional versus many-body Green's function approaches, *Rev. Mod. Phys.* **74**, 601 (2002).

[28] G. Strinati, Application of the Green's functions method to the study of the optical properties of semiconductors, *La Rivista del Nuovo Cimento (1978-1999)* **11**, 1 (1988).

[29] W. Hanke, Dielectric theory of elementary excitations in

crystals, *Advances in Physics* **27**, 287 (1978).

[30] B. Cunningham, M. Grüning, P. Azarhoosh, D. Pashov, and M. van Schilfgaarde, Effect of ladder diagrams on optical absorption spectra in a quasiparticle self-consistent *GW* framework, *Phys. Rev. Materials* **2**, 034603 (2018).

[31] K. Momma and F. Izumi, *VESTA3* for three-dimensional visualization of crystal, volumetric and morphology data, *Journal of Applied Crystallography* **44**, 1272 (2011).

[32] M. Röhlffing and S. G. Louie, Electron-hole excitations and optical spectra from first principles, *Phys. Rev. B* **62**, 4927 (2000).

[33] I. K. Turan, W. R. L. Lambrecht, and J. Jackson, Electronic structure and exchange interactions in altermagnetic mngep'2 in the quasiparticle self-consistent gw approach, *Phys. Rev. B* **112**, 144443 (2025).

[34] A. Punya, W. R. L. Lambrecht, and M. van Schilfgaarde, Quasiparticle band structure of zn-iv-n<sub>2</sub> compounds, *Phys. Rev. B* **84**, 165204 (2011).

[35] M. Cardona and M. L. W. Thewalt, Isotope effects on the optical spectra of semiconductors, *Rev. Mod. Phys.* **77**, 1173 (2005).

[36] A. Jain, S. P. Ong, G. Hautier, W. Chen, W. D. Richards, S. Dacek, S. Cholia, D. Gunter, D. Skinner, G. Ceder, and K. A. Persson, Commentary: The Materials Project: A materials genome approach to accelerating materials innovation, *APL Materials* **1**, 011002 (2013), [https://pubs.aip.org/aip/apm/article-pdf/doi/10.1063/1.4812323/13163869/011002\\_1.online.pdf](https://pubs.aip.org/aip/apm/article-pdf/doi/10.1063/1.4812323/13163869/011002_1.online.pdf).

[37] O. Dernek and W. R. L. Lambrecht, Comparison of interband related optical transitions and excitons in ZnGeN<sub>2</sub> and GaN, *Phys. Rev. B* **109**, 125133 (2024).

[38] A. Mintairov, J. Merz, A. Osinsky, V. Fuflyigin, and L. D. Zhu, Infrared spectroscopy of ZnSiN<sub>2</sub> single-crystalline films on r-sapphire, *Applied Physics Letters* **76**, 2517 (2000), <https://pubs.aip.org/aip/apl/article-pdf/76/18/2517/18548997/25171online.pdf>.

[39] N. Dadkhah, W. R. L. Lambrecht, D. Pashov, and M. van Schilfgaarde, Improved quasiparticle self-consistent electronic band structure and excitons in  $\beta$ -ligao<sub>2</sub>, *Phys. Rev. B* **107**, 165201 (2023).

[40] X. Gonze, First-principles responses of solids to atomic displacements and homogeneous electric fields: Implementation of a conjugate-gradient algorithm, *Phys. Rev. B* **55**, 10337 (1997).

[41] X. Gonze and C. Lee, Dynamical matrices, born effective charges, dielectric permittivity tensors, and interatomic force constants from density-functional perturbation theory, *Phys. Rev. B* **55**, 10355 (1997).

[42] X. Gonze, B. Amadon, G. Antonius, F. Arnardi, L. Baguet, J.-M. Beuken, J. Bieder, F. Bottin, J. Bouchet, E. Bousquet, N. Brouwer, F. Bruneval, G. Brunin, T. Cavignac, J.-B. Charraud, W. Chen, M. Côté, S. Cottenier, J. Denier, G. Geneste, P. Ghosez, M. Giantomassi, Y. Gillet, O. Gingras, D. R. Hamann, G. Hautier, X. He, N. Helbig, N. Holzwarth, Y. Jia, F. Jollet, W. Lafargue-Dit-Hauret, K. Lejaeghere, M. A. Marques, A. Martin, C. Martins, H. P. Miranda, F. Nacarato, K. Persson, G. Petretto, V. Planes, Y. Pouillon, S. Prokhorenko, F. Ricci, G.-M. Rignanese, A. H. Romero, M. M. Schmitt, M. Torrent, M. J. van Setten, B. Van Troeye, M. J. Verstraete, G. Zérah, and J. W. Zwanziger, The abinitproject: Impact, environment and recent developments, *Computer Physics Communications* **248**, 107042 (2020).

[43] M. Torrent, F. Jollet, F. Bottin, G. Zérah, and X. Gonze, Implementation of the projector augmented-wave method in the abinit code: Application to the study of iron under pressure, *Computational Materials Science* **42**, 337 (2008).

[44] <https://github.com/Electronic-Structure-Group/CaSnN2>.